VERIFICATION OF A NOVEL RABBIT MODEL USED IN THE STUDY OF HUMAN INTRACRANIAL ANEURYSM

by

Qi Yang

B.S., China Agricultural University, 2015

Submitted to the Graduate Faculty of

the Swanson School of Engineering in partial fulfillment

of the requirements for the degree of

Master of Science

University of Pittsburgh

2017

UNIVERSITY OF PITTSBURGH

SWANSON SCHOOL OF ENGINEERING

This thesis was presented

by

Qi Yang

It was defended on

April 4, 2017

and approved by

Giovanni Galdi, PhD., Professor,
Department of Mechanical Engineering and Materials Science

Sung Kwon Cho, PhD., Professor,
Department of Mechanical Engineering and Materials Science

Thesis Advisor: Anne Robertson, PhD., Professor,
Department of Mechanical Engineering and Materials Science

VERIFICATION OF A NOVEL RABBIT MODEL USED IN THE STUDY OF HUMAN INTRACRANIAL ANEURYSM

Qi Yang, M.S.

University of Pittsburgh, 2017

Coupling the hemodynamics with the pathophysiology of human intracranial aneurysm (IA) has been a subject of interest for eventually obtaining the reliable prediction of subarachnoid hemorrhage caused by aneurysm rupture. In recent works, the stability of flow patterns, regions of impingement, size of jets, wall shear stress (WSS), and the formation of vortices are considered to be the major causes of aneurysm rupture. A trending conclusion from the qualitative analysis of patient-specific cases is that aneurysms with simple stable flow patterns and large impingement region are safer than those with complex unstable flow pattern and small impingement region. When it comes to the clinic, some physical experiments such as testing of medical devices cannot be performed on patients. Thus, preclinical animal models are introduced as surrogates. In the study of human IAs, the most commonly used elastase-induced rabbit model has been found to have some limitations, in that it generates unrealistic retrograde flow inside the aneurysm. A novel method of creating bifurcation-like rabbit model for limiting retrograde flow was proposed recently and two new bifurcation-like rabbit aneurysms with different geometries were created in the Mayo Clinic. However, only the performance of one of these new cases was tested thus far. In this paper, the other novel bifurcation-like rabbit aneurysm model with an irregular long sac was investigated and its hemodynamics performance has been extensively evaluated using computational fluid dynamic (CFD) methods. The

methodology of creating this rabbit aneurysm model, the construction of the geometric model in the computer and the setting of boundary conditions is described in detail. The robustness of this rabbit model was investigated by modifying the essential geometric variables of the model. A quantitative analysis of flow pattern changes was performed to assess the robustness of the results to these changes. The results showed that this new bifurcation rabbit model is capable of generating two important flow types and these flow types are robust to geometric perturbations. The results of this thesis serve as additional evidence that the novel bifurcation-like rabbit model has great value and relevance for understanding the impact of flows found in human aneurysms.

TABLE OF CONTENTS

LIST OF TABLES

LIST OF FIGURES

PREFACE

I will firstly send appreciation to my committee members, Dr. Giovanni Galdi, Dr. Sung Kwon Cho and Dr. Anne Robertson for their efforts and contribution towards this thesis. This work is impossible to be finished without their insightful suggestions. I am so lucky to obtain valuable contributions from the following people and grant.

I would like to thank my thesis advisor Dr. Anne Robertson for the every effort she made to help me polish this thesis. The door to Dr. Robertson's office was always open whenever I ran into a trouble spot or had a question about my research or writing. She consistently allowed this paper to be my own work, but steered me in the right the direction whenever she thought I needed it. Though an incredible daily schedule she had, she still would manage time for discussing in person with me. What she has done for me are invaluable and precious.

Michael J Durka, who is a Phd candidate in our group, helped me unconditionally with this work. Before I entered the group, my background in human intracranial aneurysm and hemodynamics are limited. Without his help, I could not catch up so quickly and finish the thesis with such a limited time. He was both a good teacher and a supportive friend for me.

Dr. Cebral and his collaborators at George Mason University provided the commercial solver in this study and Dr. David Kallmes and collaborators at the Mayo Clinic provided the method of creating rabbit models.

Qiaoyi Wei, a master student majoring in Material Science, always comforted me when I was in the fear of missing the deadline of this thesis. Without her support, the whole journey would be so scary and painful.

In addition, we appreciate the support from the National Institute of Neurological Disorders and Stroke (NINDS) and the National Institutes of Health through the grant No. 1R21NS088256: Translational, Multimodality Correlation between Human and Rabbit Saccular Aneurysms.

Finally, I must express my very profound gratitude to my parents and for providing me with unfailing support and continuous encouragement throughout my years of study and through the process of researching and writing this thesis. This accomplishment would not have been possible without them. Thank you.

1.0 INTRODUCTION

An intracranial aneurysm (IA) is a saccular dilation in the human blood vessels and believed to arise from flow derived changes in the arterial wall. As the main cause of non-traumatic subarachnoid hemorrhage, IA is sometimes viewed as a silent bomb that would kill people unpredictably. In North America, 5 out of 10 people die because of subarachnoid hemorrhage and an additional 20% of patients are plagued with sequelae. However, compared with the mortality, the possibility of the rupture of an IA is surprisingly low. According to the International Study of Unruptured Intracranial Aneurysm (ISUIA) in 2003, the rate of rupture is in the range of 0.1% to 1% depending on the size and the location of the aneurysms. In Brown and Broderick's study of unruptured aneurysms, they found the likelihood of 5-year cumulative rupture of small aneurysms, namely aneurysms <7 mm in diameter, was almost zero when they developed in the anterior-circulation or in the cavernous carotid artery [1]. Jeong, Jung and Kim reviewed 239 ruptured aneurysms and found that ruptured aneurysms in the anterior communicating artery were on average smaller than those are in the middle cerebral artery. Therefore, it is often recommendations for treatment should be made in accordance with the location of the aneurysm [2].

The major guidance for predicting the rupture of an aneurysm is based on aneurysm size [3], and a large number of patients with small IA are not recommended for any treatment. However, it has been shown in clinical studies that even though the likelihood of rupture is less

for small aneurysms, the sheer number of small aneurysms makes this group a substantial contributor to the ruptured population. In a result, the size of the aneurysm alone is not sufficient for rupture risk assessment. In 1999, Ujiie firstly correlated aspect ratio (AR: the ratio of aneurysm depth to aneurysm neck width) with the likelihood of aneurysm rupture. Once the AR was larger than 1.6, a secondary low circulation flow zone in the IA sac, near the dome region. This flow feature was conjectured to be important factor for rupture in aneurysms. Later in 2004, Nader verified the reliability of the AR for predicting the rupture of aneurysm. 182 aneurysms were analyzed in 75 patients with subarachnoid hemorrhage by examining the angiographic films. Statistical result showed that the mean AR for 75 ruptured aneurysms were 2.7 while that for 107 un-ruptured aneurysms were 1.8. Although Nader's research did not provide a critical AR, the results suggested that aneurysms with higher AR were more likely to rupture so that extra attention and treatment are needed for patients with high AR aneurysm. Sufficient researches made the AR and the size of aneurysm the most commonly used variable in the study of aneurysm rupture prediction.

In recent years, in addition to AR and size of aneurysm, more and more factors have been considered for enhancing the accuracy of rupture prediction. Gathering some current prevailing theories, the region of impingement (the region where the flow impinges against the aneurysm wall), size of flow impingement region (IS: the region was classified small or large with respect to the area of the aneurysm sac), aspect ratio (AR: the ratio of aneurysm depth and aneurysm neck width), wall shear stress (WSS: the time averaged projection of Cauchy stress vector from the flow on the endothelium) and the stability of flow patterns are believed to have considerable effects on aneurysm rupture. Baek et al. analyzed flow in patient-specific geometric models of the supraclinoid internal carotid artery (ICA) with posterior communicating artery (PCoA) and

found the flow impingement at the aneurysm wall created a high pressure region surrounded by high wall shear stress area. In this study, the impingement region was found to coincide with the location of the rupture of aneurysm [4]. However, the rupture site and impingement point is not always consistent. Wall shear stress magnitude is a common focus of computational studies of flow in the aneurysm sac due to the well-known connection between flow and cellular dysfunction that can prevent effective wall maintenance [5]. Mostly in the circle of Willis, the range of shear stress falls in the range of 0.4-7.0 Pa. At the locations where endothelium is exposed to abnormally low or high wall shear stress, proteolytic and oxidative damage can be induced. Exposed to such chemical damage, the aneurysm wall can degrade, and potentially rupture. Although the high and low WSS are both associated with rupture of aneurysms the mechanisms of degrading process have been found to be significantly different. Low WSS is responsible for an inflammatory-cell-mediated pathway, which can cause thickening of the endothelium and lead to rupture of atherosclerotic aneurysm. Once the inflammatory response is triggered by the low WSS, reactive oxygen chemicals are produced in the endothelium and the permeability of the luminal layer is increased. This dramatically facilitates the migration of leukocyte from blood into vessel wall and proceed to elicit an increase in matrix metalloproteinases, a key factor of wall degradative process [6]. High WSS is thought to cause a mural-cell-mediated pathway. When the shear stress exceeds the critical threshold, the number of local proteases are dramatically increased and activated by intramural cells. The production and activation of local proteases cause the attenuation of the aneurysm wall and can eventually lead to the rupture of the aneurysm.

It is more convincing that the rupture of aneurysm is caused by a combination of flow factors. In Cebral's study of characteristic hemodynamics, the aneurysms have been firstly

classified into four different types based on the stability and complexity of flow patterns, size of the impingement region and the concentration of inflow. Type I—unchanging direction of inflow jet with a single associated vortex; Type II—unchanging direction of inflow jet with multiple associated vortices but no change in the number of vortices during the cardiac cycle; Type III—changing direction of inflow jet with creation of a single vortex; and Type IV— changing direction of the inflow jet with creation or destruction of multiple vortices [7]. A common conclusion is that aneurysms with simple stable flow patterns and large impingement regions are safer than those with complex unstable flow patterns and small impingement region. This qualitative study of characteristic hemodynamics has strongly facilitated and motivated the understanding of the initiation, development and rupture of human IA.

This prior work was a qualitative study correlating hemodynamics and aneurysm pathology. Since the rigor and integration of subjective analysis could be affected by personal bias, it is desirable to employ a more objective quantitative analysis for hemodynamic classification. Cebral et al built on his prior qualitative characterization and introduced a flow characteristics that could be assessed using an automated, user independent, method. In particular, he introduced the Proper Orthogonal Dimension method (POD) and vortex core line length as metrics of complex flow inside human IA. It has been shown that ruptured aneurysms have, on average, larger values of the POD number and longer vortex core line lengths [8]. Additional quantitative parameters, such as inflow concentration index (ICI) and shear stress concentration index (SCI), were also extracted from computational simulation results and investigated for their relationship with aneurysm rupture. Investigation of the relationship between IA rupture and flow parameters of this kind continues to be an active area of investigation.

While the results highlight the significances of correlating the characteristics hemodynamics and the rupture of cerebral aneurysm, it also identified the potential for computational fluids dynamics to serve as a powerful tool in the study of humane IA. Unfortunately, the metrics of the complexity of the flow cannot be measured using existing experimental techniques. Faced with this challenge, researches take CFD simulation as a reliable method to estimate hemodynamics inside aneurysms.

Furthermore, there are new medical devices for treating aneurysms that function by altering the blood flow. An important area of research is the direct evaluation of how the flow impacts the walls of control blood vessels and aneurysm domes. Such studies cannot be performed in humans. 3D geometric CFD models are built by taking references from preclinical animal models. Experiments on these animal models, such as testing aneurysm occlusion devices [9] or designing new flow-diverter [10], provide useful information which significantly facilitate the development of intracranial aneurysm treatment. The most frequently used models were dogs, rabbits, rodents and swine. Elastase-induced rabbit saccular aneurysm is one of the best models for reproducing the morphology of human intracranial aneurysm [11].

3D models of the lumen are needed for the CFD studies. They are built from patient specific data obtained from computed tomography (CT), 3D rotational angiography (3DRA) or magnetic resonance imaging (MRI) [12][13] [14]. Sensitivity studies of the extent of the vascular domain on the CFD results have been performed to understand the balance between time efficient models and model accuracy [15]. The choice of the boundary condition also plays a paramount role for obtaining accurate and valid CFD results [16]. Along with the rise of CFD in medical fields, some questions and doubts about the accuracy of the CFD have arisen and thus limit the application of CFD by physicians to aneurysm treatment [17]. In 2013, the International

CFD Rupture Challenge was introduced to evaluate the accuracy and consistency in CFD results obtained from different research groups using diverse computational approaches. The results showed that over 80% of the participating groups generated similar flow predictions regardless of the variations in numerical schemes, mesh resolution and solvers [18]. While such studies are in some sense encouraging, there is also a need for a more robust gold standard when evaluating the quality of numerical analysis across research groups. For example, more recently, concern has risen that high frequency instabilities exist in the aneurysm dome and may have been missed in earlier studies that did not have sufficient spatial or temporal resolution.

For investigating the pathophysiology of cerebral aneurysms and aiding the design of effective treatments, preclinical animal models are important, if not essential. The animal models of saccular aneurysms have been improving in recent years, though there remains a great need for validation of their relevance. Elastase-induced rabbit model is one of the most commonly used model for in vivo experiments [19][20][21]. The Kallmes group developed an elastase induced aneurysm model in New-Zealand white rabbits in which the saccular aneurysms are generated on the right common carotid artery (RCCA) using elastase infusion. In particular, a balloon catheter is used and swine elastase is delivered to induce dilation of the lumen of the proximal RCCA. Then the RCCA is ligated at the midpoint and the stump of RCCA forms an artificial aneurysm [22]. This is a sidewall aneurysm model that has been shown to have a good match with geometry and many flow features of human aneurysms.

However, due to the proximity of the model to the heart, a retrograde flow condition, which is unlikely to appear in human brain, is generated inside this model. In addition, only a single flow type of those introduced by Cebral et al. is generated within this model. Unfortunately, this single flow type is less clinically important than the other three flow types

that are commonly found in human IA by Cebral. To increase the value of this model there is a need to create new models with solely prograde flow and bifurcation type geometry and a larger range of flow types.

Noting that the human brain is distant from the heart, it is more realistic to create a fully prograde flow inside the aneurysm sac. In this thesis, a novel fully prograde bifurcation type rabbit model generated by Mayo Clinic and is shown to have the potential of providing more clinically related flow types. With the aid of computational simulation, the flow patterns that could generated by this new model was visualized and the characteristic parameters were calculated. For verifying that more similar flow patterns were produced, Cebral's classification of flow type was taken as a reference.

Additionally, the robustness of this new model to geometrical variation was investigated by modifying critical shape parameters. Originally, two test cases of bifurcation model (Test Case 1 and 2) and one test case of sidewall model (Test Case 3) were made. The central difference between Test Case 1 and 2 is related to the aspect ratio of the dome. Test case 1 has a lower aspect ratio and is geometrically more similar with natural human IA, Test Case 2 has a very high aspect ratio. Besides the difference in geometry, the impingement regions of the inlet flow for Test Case 1 and 2 were the dome region and neck region representatively. The Test Case 3 was created using the earlier sidewall technique and used here as a reference geometry. As a second part of this study, geometric perturbations were made to test the robustness of this new bifurcation model to variations arising during creation.

An important finding of this work is that Test Case 1 and 2 could successfully generate both Type 1 and Type 2 flows. These types are commonly observed in human IA. Another important finding is that modest changes in aneurysm geometry and aneurysm orientation

(inclined aneurysm) relative to the parent artery, such as might occur during aneurysm formation, did not cause a change in flow type. Quantitative parameters including POD number, value of POD, core line length and mean WSS, were provided for further study.

2.0 OVERVIEW OF THE ANIMAL MODELS USED IN HUMAN IA STUDY

For better understanding of the initiation, growth and rupture of human intracranial aneurysms, in vivo experimentation is necessary. In this chapter, an overview of the animal models used in the study of human IA is given. Also, the details of the different methods for generating the rabbit model are given. A new rabbit model, which is created to contain prograde flow, is introduced as an advanced model for better representing the characteristic flow inside human IA. This model arises from the Kallmes group, who are collaborators on this work.

2.1 ANIMAL MODELS

Animal models play an extremely important role in the scientific study of the pathology of human aneurysms and are also important for testing of related medical devices. Generally, there are four types of animal models applied in medical study: spontaneous, induced, negative and orphan [23]. The first two methods are more frequently used than the other two models. Spontaneous model refers to animals that naturally develop a disease with similar pathogenesis and symptoms. However, the rate of aneurysms that spontaneously occur in animals is extremely low. In order to provide animal model aneurysms in sufficient numbers, induced models are introduced. The basic idea of these models are to manually generate aneurysms using physical, chemical or biological inducement [24]. One of the biggest advantage of this method is that the

location, size and even the geometry of the aneurysm could be customized according to different research purposes, which strongly facilitates the study of saccular aneurysms.

Different animal model were chosen for satisfying different studies. Small animals like rats or rabbits are frequently chosen for scientific experiments. For example, elastase-induced rats model was generally used for the study of the mechanism of aneurysmal enlargement [25]. Ciprian used elastase-induced rabbit model aneurysm for testing asymmetric vascular stent [26]. Under some rare circumstances, large animals such as monkeys or dogs are also used. Zarins and co-workers used cynomolgus and rhesus monkeys for investigating atherosclerosis and atherosclerosis regression [27]. Yan and Zhu tested a distal internal carotid artery aneurysm in dogs, which prove solid evidence that dog model could represent considerable similarities in geometry and hemodynamics with humans [18]. Although there are no certain rules for selecting animal model, three general principles were given by Oliveira [22]: 1) The type of animal to use; 2) The type of aneurysm to study; 3) The research purpose of the study. No matter what animal to use, it is important to thoroughly understand the biological characteristic (such as size and metabolism), vasculature and the level of similarity (if the animal result could be extrapolated to be useful for human). When the level of similarity is equal, large animals like pigs or monkeys are less ideal than small animals due to ethical considerations and cost. Compared with small animals, it obviously takes more human effort to feed, lodge and care for large animals. Considering the reasons above, only a small group of large animal objects is normally used which will result in less statistical significance and potentially lead to inaccurate conclusions. For this reason, we focus on the rabbit model in this study.

2.2 DIFFERENT METHOD OF CREATING SACCULAR ANEURYSM

2.2.1 Surgical method

The experimental aneurysm models could be classified into four types: 1) Chemical induced aneurysms, created by injecting caustic substances such as hypertonic saline, pancreatic elastase and nitrogen mustard; 2) Laser induced aneurysms, formed by laser-sealed arteriotomy; 3) Combined inducement triggered aneurysms, formed by the combined effects of carotid occlusion, induced lathyrism and induced hypertension; 4) Surgically created aneurysms, formed by creating a venous pouch on an artery [28].

2.2.2 Elastase-induced method

While there is no animal model that can perfectly reproduce all the hemodynamic and geometric features of human intracranial saccular aneurysms, they have different areas where they can be used to effectively for scientific and medical studies. Elastase-induced models have been recognized as another efficient method for creating saccular aneurysms. Rats, rabbits and dogs are used for elastase models. Although no agreement has been reached on which is the best animal model, the rabbit model has a coagulation system with important similarities to that of humans[29].

In the past few decades, the elastase-induced rabbit method has been improved and optimized. A sidewall rabbit aneurysm model was created by Cawley and coworkers in 1996. Although the geometry of this rabbit aneurysm model was similar with that in humans, it failed to represent similar hemodynamic features with humans since the lumen is considerably

damaged [30]. Then in 1999, Cloft and colleagues made a more reliable rabbit model based on Cawley's work with higher hemodynamic stresses using the left common carotid artery (LCCA). Briefly, a small arterial segment on the LCCA was isolated and then exposed to pancreatic elastase for 30 minutes. Compared with the aneurysm models created using Cawley's method, the new aneurysm models are consisting in size. Additionally, the endothelium in these models is largely intact, providing an opportunity to study the effect of changing hemodynamic conditions on the endothelial biology [31]. While the method of creating this sidewall aneurysm model was established and developed, it was acknowledged that bifurcation and terminal aneurysms are more common in humans than sidewall aneurysms. More recently, Kallmes's group successfully built on their earlier work with Cloft to create a bifurcation aneurysm model by manipulating the right common carotid artery (RCCA). The location of RCCA is between the aorta and brachiocephalic artery which is shown in Figure 1. The long curvature of brachiocephalic helps to provide a higher hemodynamic stress environment at the proximal of RCCA.

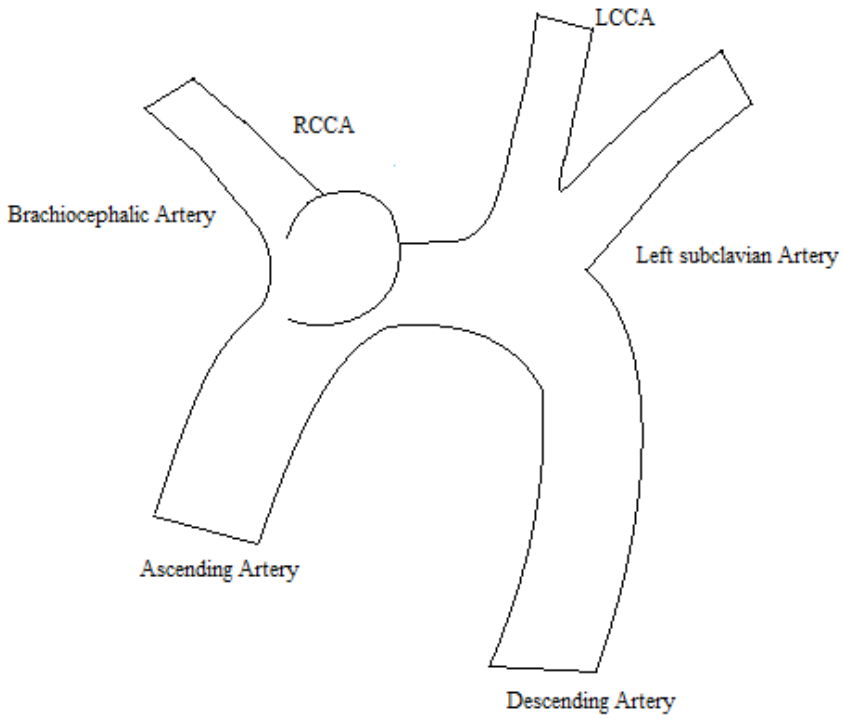

Figure 1. The Kallmes bifurcation rabbit model

One drawback of forming a model aneurysm close to the heart, is that the flow in the rabbit aneurysm is partly retrograde. Namely, during the systolic period, the blood flow is one-directional inside the vasculature. During diastole, back flow can appear and the direction of the flow inside the sac can change rapidly. This flow is different from that in the brain which is remote from the heart. The elasticity of the arteries near the heart modify the waveform and consequently, the flow is prograde inside human aneurysms. Thus, the flow in the rabbit models have some differences with that in human IAs even though many metrics of the flow have been shown to be similar[21]. In order to solve this problem, a new rabbit model which could provide more similar flow condition with humans has been created by the Kallmes group. In the following section, the methodology for creation of this new model will be described in detail.

2.2.3 New advanced rabbit model

A novel bifurcation rabbit model was created using New Zealand white rabbit at Mayo Clinic [32]. The saccular aneurysms were created in the proximal LCCA with distal ligation and further elastase injury. For generating the fully prograde condition, the RCCA was directly attached to the venous system to produce a high flow environment. As will be shown in the remainder of this thesis, using in silico modeling (CFD), this new model can generate two additional flow types: Type 1 and Type 2 flows. The sidewall aneurysm created by the previous protocol only generated Type 3 flows. Among 62 patient-specific aneurysms, Cebral classified the flow types and reported that 44% were Type 1 flow while only 17% were Type 3 flow. Type 4 and Type 2 flow were 20% and 19% representatively. Thus, Type 1 flow is the most commonly observed flow type and of great value to study. Since the new bifurcation rabbit model can provide more additional and common flow types, it has potential to serve as a valuable tool in the study of relating characteristic flow with wall structure.

3.0 COMPUTATIONAL SIMULATION OF FLOW IN THE RABBIT MODEL

Intracorporal testing on the human body or human organs is highly controlled and only allowed after a careful balance of the benefits to risks. This restriction must be respected and followed, but it causes difficulties to testify the reliability, compatibility or therapeutic efficacy of a medical device, which would also threaten the life security of patients. For solving this problem, preclinical animal experimentation is normally required before any medical device can be used in the clinic. Therefore, attention must be paid to the human relevance of the animal model which is one of the most important preconditions for obtaining any convincing results and extrapolating the conclusion to humans. In the study of human IAs, poor ability of animal model to represent characteristic flow patterns in human aneurysms could cause important errors in the design of medical devices. Using computer aided methods, it is possible to simulate the internal flow condition inside the animal model and use this information to assess the similarity in flow between animal models and human IAs. In the following sections, the whole process of simulating flow in the rabbit aneurysm model will be given in detail.

3.1 CONSTRUCTION OF THE COMPUTATIONAL MODEL

Commonly, the reconstruction of realistic 3D models for numerical calculation are largely from medical images such as computed tomography arteriography (CTA), magnetic resonance angiography (MRA) and three dimensional rotational angiography (3DRA). Contrast agents are injected into target areas to make vasculature stand out from the surrounding biological tissues. Normally blurry and gross, the initial images require further image processing, such as cropping, contrast enhancement (sharpening) and reducing blur (smoothing). Using 3DRA, tens of thousands of points are recorded to define the lumen surface and used to create a 3D model. However, abundant points are inevitably included in the dataset and thus rendered the efficiency of manipulating the control domain in some extent. Thus, a parametric modeling method has been created to facilitate the reconstruction process by defining systematically controllable point set[33]. Centerline points are first sorted out from the original dataset and used to form an initial framework of the model. The best fit diameter of the vessel are then defined as 2D vessel slices and imposed normal to the centerline to capture the curvature of the original surface. Finally, the surface of the 3D model is constructed by sweeping along the circular cross-section series. Although the parametric modeling method could improve the quality of the 3D model and be beneficial for saving computational time, the model is also under the risk of oversimplification. Extra attention must be paid when manually picking up the centerline points and measuring the best fit of vessel diameters in order to maintain the characteristic features of the original model.

The model is expected to contain the major vasculature features although subtle branches and surface irregularities are inevitable. These nonideal surfaced features can cause raised edges, element overlap or topological defects when generating the finite element mesh. Failures in grid generation could result in large consumption of computational time and even impede the

numerical computations. To improve the effectiveness of the computations, smoothed and refined surface conditions are applied though they will affect the hemodynamic results to some degree. Additionally, the extent of the vasculature upstream and downstream of the aneurysm that is included in the computational model has been shown to affect the hemodynamic results. Changes in the length of upstream and downstream arteries, the number of branches connected with the parent artery and the involvement of aortic arch could lead to unreliable CFD results. In Zeng et al research, the sensitivity of CFD results to idealized vasculature of rabbit model was investigated [15]. Their results demonstrated that flow in the high AR model was less sensitive to the extent of the vasculature than the low AR model. As a consequence, it was possible to use a simplified model yet still maintain a good accuracy in the WSS results. For the low AR case, as long as the downstream vasculature was untouched, the CFD results would still be reliable.

3.2 MODELING THE BLOOD

3.2.1 The mechanical properties of blood

Blood is recognized as a colloid suspension which is mostly water but also contains proteins, hormones, dissolved oxygen and carbon dioxide, mineral ions and blood cells (red blood cells, white blood cells and plaques). The typical values for human blood density is ρ=1150 kg/m3 and high shear viscosity is μ=0.04 mPa. Blood is 92% volume of water (including the interior of the red blood cells), and therefore blood is usually modeled as an incompressible fluid[34]. If the blood cells are excluded, the liquid part of blood, which is called plasma, behaves like a Newtonian fluid. However, blood is a multi-phase fluid with cells occupying 40-45 of the

volume. Nonetheless, well stirred blood behaves approximately like a single phase constant viscosity fluid for flow in arteries. When the diameter of vessel is on the same scale with blood cells such as in capillaries, or even an order of magnitude larger than this, such as in arterioles and venules, the multi-phase nature of blood plays an important role in determining the mechanical response of blood. It is no longer well modeled as a single phase constant viscosity (Newtonian) fluid. In the capillaries, the flow is often modeled as a Stokes (noninertial) flow and the behavior of individual red blood cells is considered. When simulating animal blood, the rheological model is also chosen according to the scale of vessels but the values of blood properties are decided by the animal species.

3.2.2 The velocity profile of blood flow

As the beating of the heart and the resistance from the artery wall, the blood inside vessel is changing in velocity and orientation periodically, namely pulsatile. In a straight pipe, the solution for pulsatile (time periodic) fully developed flow a Newtonian fluid in a straight pipe of circular cross section is

$$u(r,t) = Re\{\sum_{n=0}^{N} \frac{iP'_n}{\rho n\omega}[1 - \frac{J_0(\alpha n^{1/2} i^{3/2} \frac{r}{R})}{J_0(\alpha n^{1/2} i^{3/2})}]e^{in\omega t}\} \quad \textbf{(3-1)}$$

Where u (r, t) is the transient axial component of the flow velocity in cylindrical coordinates, α is the Womersley number, Re{} is the real part of a complex number, n are the natural numbers, i is the imaginary number, P'_n is the pressure gradient magnitude for the angular frequency nω, ω

is the angular frequency of the first harmonic of a Fourier series of an oscillatory pressure gradient, $J_0()$ is the Bessel function of first kind and order zero and R is pipe radius.

The Womersley number is an important dimensionless number, defined as

$$\alpha = R(\frac{\omega\rho}{\mu})^{1/2} \quad \textbf{(3-2)}$$

From the equation above, we can tell that Womersley number represents the ratio of transient inertial force and viscous force. When α is no larger than 2, viscous force is dominant and the velocity profile is approximately parabolic. When α is larger than 2, inertia force gradually dominates the flow in the central core while viscous forces still have strong effect on the boundary layer. The velocity profile gets flattened when α gets larger.

However, the spatial velocity profile in the cross section of the vessel is strongly affected by its distance from the heart. In arteries that are straight and long, the blood is sometimes modeled using the first order Womersley approximation (FOW). The FOW approximation is formed from one steady term (Hagen-Poiseuille flow) and one first order unsteady term from the velocity field above, so that it could provide more accurate results than the simple steady approximation using the Hagen-Poiseuille parabolic velocity profile. Furthermore, at the location where blood is leaving the heart, the spatial velocity profile is reported to be more like a time varying uniform profile [35].

3.3 BOUNDARY CONDITION

In this work, blood flow is governed by the three dimensional time dependent Navier-Stokes equation. Five different combinations of inlet/outlet boundary condition are normally used in solving the governing equation and are given in Table 1.

Table 1. Different combination of inlet/outlet boundary condition

Model	Inlet	Outlet
V-NS0	Fully developed velocity profile with pulse waveform	Zero normal stress condition
P-V	Time dependent pressure waveform	Scaled fully developed velocity profile with pulsatile waveform
V-P	Fully developed velocity profile with pulse waveform	Time dependent pressure waveform
P-P	Time dependent pressure waveform	Time dependent pressure waveform
P-NS0	Time dependent pressure waveform	Zero normal stress condition

Liu, Zheng and Bach evaluated the above five inlet/outlet boundary condition in a stenotic coronary artery by investigating their effects on velocity magnitude, wall shear stress, pressure drop and the spatial gradient of wall pressure. While significant variation is caused in temporal distributed velocity magnitude and maximum wall shear stress, the type of boundary condition applied at the inlet and outlet did not generate considerable effect on the pressure drop,

the wall pressure gradient and the wall shear stress [36]. In the study of human IA, V-NS0 model is the most commonly used boundary condition when the pressure waveform is not available. Typically, one of the downstream outlets would be prescribed as “traction free” while transient velocity boundary conditions are applied at the other inlet/outlet boundaries.

3.3.1 Velocity boundary condition

Ideally, the prescribed velocity boundary conditions are based on measurements of flow rate at each branch obtained from measurements such as intravascular duplex Doppler measurement. However, under some circumstances such that the size of vessel is too small or the surrounding vasculature is too complex, physical measurements do not provide clear velocity information. In such situations, parametric studies can be used.

In 1926, the physiologist Cecil Murray concluded that the cube of the radius of parent artery should be equal to the summation of cubes of radii of the daughter arteries. This result is commonly referred to as Murray’s law and can be written as:

$$R_k{}^3 = \eta R_{k+1}{}^3 \quad \textbf{(3-3)}$$

where R_k is the radius of parent artery and R_{k+1} are the braches that the parent artery splits into. This relationship is obtained by minimizing the cost function which is related to the sum of the work done by the blood and the metabolic rate of the blood inside the vessel [37]. Later in 1995, Ghassan and Fung showed that Murray’s law could also be derived as a result of assuming

constant wall shear stress and following the conservation of mass and momentum. Also, the hypothesis of constant wall shear stress is supported by several independent research group [38]. For steady, unidirectional velocity fields, the wall shear stress is inversely proportional to the cube of vessel radius:

$$\tau = \frac{4\mu Q}{\pi R^3} \tag{3-4}$$

where μ is the viscosity of blood, Q is the flow rate and R is the radius of the vessel. This equation is obtained under following hypotheses: 1) the blood is modeled as incompressible Newtonian fluids which implied that the fluids is under the government of Navier-Stokes equation; 2) the artery wall is modeled as no-slip rigid wall; 3) the vessel is assumed to be ideally straight circular tube; 4) the blood is one-dimensional (only in axial direction) laminar flow.

According to the hypothesis of constant wall shear stress, the flow rate of unknown vessel can be estimated. For example, the WSS at the entrance of the ascending artery and outlet of the descending should be equal to each other. Thus we should have:

$$\frac{4\mu Q_{asc}}{\pi {R_{asc}}^3} = \frac{4\mu Q_{des}}{\pi {R_{des}}^3} \tag{3-5}$$

After crossing out the same components on the left and right side, the equation becomes:

$$\frac{Q_{asc}}{Q_{des}} = \frac{{R_{asc}}^3}{{R_{des}}^3} \quad \textbf{(3-6)}$$

Where Q_{asc} could be obtained by the duplex Doppler measurement, R_{asc} and R_{des} are automatically measured in the CFD analysis software. Thus, we can calculate Q_{des} out and prescribe it at the boundary of the descending artery.

3.3.2 Traction Free boundary condition

For solving flow in the vasculature, usually a traction boundary conditions are prescribed for at least one of the inlet/outlet conditions. A zero normal stress condition, which also noted as "traction free" boundary condition, is frequently. Under the assumption that the downstream vessel is sufficient long and straight, the flow can be approximated at fully developed. The pressure is only determined up to a function of time in the Navier-Stokes equations. Without loss in generality the pressure at one point in the domain can be set equal to zero. Therefore, the traction boundary condition reduces to the condition that the gradient of the normal component of velocity is zero. While this is satisfied in the flow direction due to the fully developed flow, it does impose a condition that is inconsistent with even the Hagen-Poiseuille solution for fully developed flow in a pipe. For example, using cylindrical coordinates with z-axis aligned with the centerline, the zero traction condition would imply that τ_{rz} is equal to incorrect. Generally, for simplicity, this condition is nonetheless used, and appears to be accepted away from the inlet/outlet where it is applied.

3.3.3 Modeling of arterial wall

Modeling of arterial wall is a challenge in computational mechanics due to the complexity of arterial wall structure, the coupling to the blood flow and the uncertainty of arterial wall material properties. The arterial wall, which consists of cellular (e.g. vascular smooth muscle cells) and extracellular material (e.g. collagen fibers) is often modeled as a nonlinear hyperelastic material. When the blood is flowing through the artery with pulsatile pressure, the wall will correspondingly dilate and contract displaying a coupling between blood and wall motion. This behavior is referred to as Fluid Structure Interaction (FSI). Since around the turn of the century, computational approaches have been developed to model FSI and this topic is still an area of intense investigation. Nonetheless, the rigid wall assumption is still widely used. In the few past decades, the advances in computational fluids dynamics and computational power make it possible for FSI model to be used in the study of arterial wall mechanism. Models that include wall deformation are more realistic compared with rigid wall models, though like any modeling complexity, it is important to understand under what conditions it is needed. Siogkas and co-workers investigated the effect of including FSI in models by comparing results for the rigid wall model for the average WSS as well as low WSS. The result of two models showed evidently good agreement for the average WSS on a certain length of arterial segment. For the area of low WSS, the results generated by the two methods are qualitatively and quantitatively similar at the same time [39]. Thus, different wall models could be chosen for different cases while the accuracy and consistency of results are preserved.

4.0 VALIDATION OF THE NEW RABBIT MODEL FOR THE HIGH FLOW, HIGH ASPECT RATIO ANEURYSM

4.1 ABSTRACT

Following the idea of creating a high pressure rabbit aneurysm model in vivo, two bifurcation-like aneurysms, denoted as Test Case 1 and Test Case 2, have been generated in New Zealand white rabbit in Mayo Clinic. Test Case 1 has a more generalized shape and size of sac compared with Test Case 2 which was created with an exceptionally high aspect ratio (AR=2.7). Test Case 1 was shown to be capable of producing both Type I and Type II flows regardless of the AR of the sac in the previous study[40]. The testing result has significant meaning in clinical study since Cebral had previously pointed out that Type I and Type II flows are frequently observed in human sidewall and bifurcation aneurysms. Additionally, the flow type generated in the Test Case 1 model was found to be robust to perturbations in geometry and direction of the aneurysm. However, it is not convincing to have only one successful case for introducing a new model into a scientific study. In this study, the flow types that can be generated by Test Case 2 are investigated to see if this new flow bifurcation model can also generate Type 1 flow, Type 2 flow or both. Similarly, the robustness of Test Case 2 is also tested using the same methodology used in Test Case 1. As described below, our results show that Test Case II can generate both Type 1 and Type 2 flows just like Test case 1 under conditions of low and high flow, without being

affected by the irregular geometry. Furthermore, the flow types in Test Case 2 are also robust to geometric and directional perturbations. In the following sections, the methodology and the computational results obtained for Test Case 2 are given in detail.

4.2 METHODOLOGY

Test Case 2 was created following the same method used for Test Case 1 as described in Section 2.2.3. The central difference between Case I and II is that the location of ligation on the LCCA in Test Case 2 is further from the proximal LCCA. In this study, 3D models of rabbit vasculature were reconstructed using a commercial package (MIMICS; Materialise, Leuven, Belgium) based on 3DRA data. The original models were then refined within another software (Geomagic; 3D Systems, Morrisville, North Carolina) to get rid of rough surfaces, irregular small bumps and redundant subtle vessels. In addition, the vessels were slightly trimmed in order to obtain flat boundary edges when modeling the surrounding vasculature. All of the refinements were done under the guidance of sensitivity studies to check the impact of idealizing the surrounding vasculature for the rabbit aneurysm model. When smoothing the surface, an automatically relaxing tool can be used, though a careful check must be made to ensure it does not cause a change in the volume of the sac. In cases where the volume would be changed when using this tool, the surface needs to be smoothed manually according to use sandpaper tool and spike removing tool in Geomagic.

Test Case 2 was originally made with high AR. Since AR is acknowledged as one of the most important factors for hemodynamic characteristics, both low AR and high AR aneurysm were investigated here. Namely, methods have been developed at the Mayo Clinic to control the

aspect ratio of the aneurysm model[41]. Here we use our custom software to create parametric models of aneurysms to generate a low AR (AR=0.95) model which maintains the same values for chosen sac geometric parameters (the maximum width of neck region, orientation of the sac and the surrounding vasculature) to be identical with the original model. Our parametric approach makes it possible to run a systematic study of the role of geometric parameters, where one parameter is changed at a time. Therefore, the flow patterns formed in a set of different AR cases can be obtained and analyzed for identifying the role that AR plays in effecting characteristic hemodynamics. The geometry of both high AR and low AR cases are shown in Figure 2.

While the Mayo Clinic has developed methods for controlling the aspect ratio of the sac and some other geometric parameters, there are limitations to how precisely these parameters can be controlled. Therefore, it is important to assess the robustness of flow type to changes in aneurysm geometry. To achieve this objective, CFD was used to study flow inside sacs with two types of geometric modifications- changes in bottle-neck and also to inclination of the aneurysm sac to the central plane of the aortic arch. The bottle-neck parameter was changed by narrowing the neck and expanding the maximum width of the original aneurysm simultaneously. The inclination of the aneurysm sac was altered by rotating the neck plane of the aneurysm. For example, Figure 3 and 4 show the variation between original and modified aneurysm in Test Case 2 for both high AR and low AR case. The aneurysm with a modified bottleneck factor is denoted as Mod A and the model with a modification to the sac orientation relative to the parent plane (increased inclination) is denoted as Mod B.

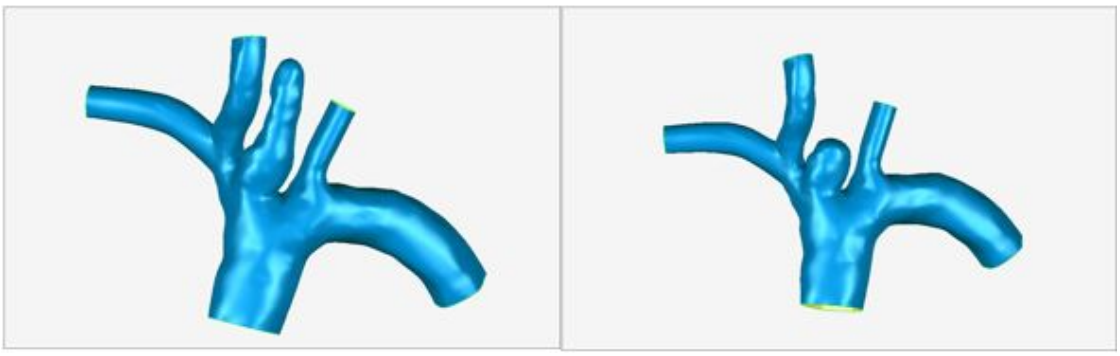

Figure 2. Test Case 2 showing original geometry (left) and low aspect ratio sac (right) that was designed using our inhouse parametric code.

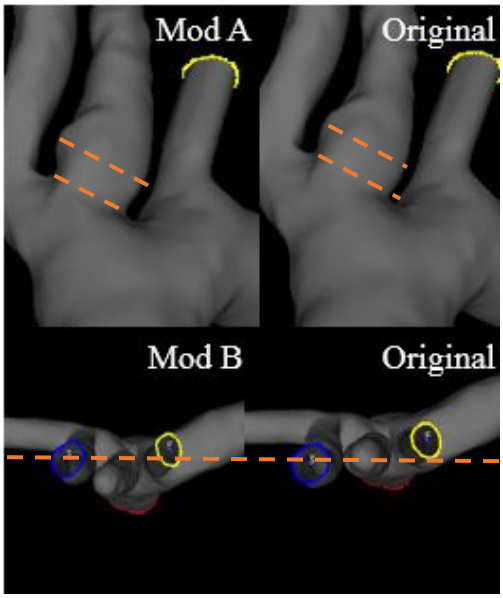

Figure 3. Left column: The original geometry of high AR Test Case 2; Mod A: Bottlenecked high AR aneurysm; Mod B: Inclined high AR aneurysm.

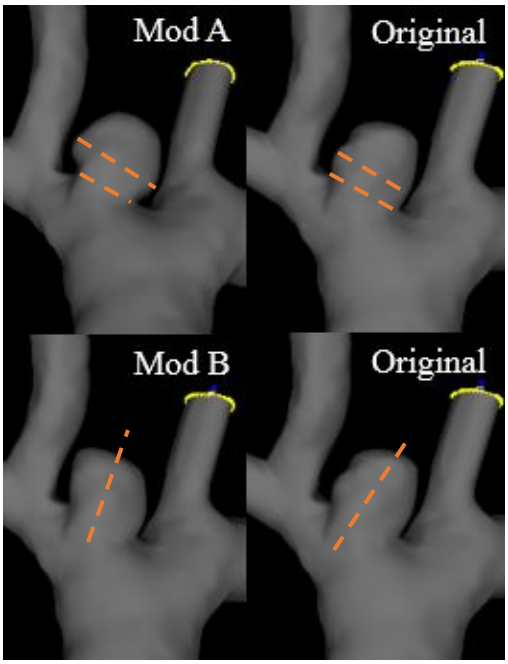

Figure 4. Left column: The original geometry of low AR Test Case 2; Mod A: Bottlenecked low AR aneurysm; Mod B: Inclined low AR aneurysm.

For reasons motivated in the methods chapter, the blood was modeled as an incompressible Newtonian fluid with constant density ρ=1050 kg/m^3 and constant viscosity μ=0.35 mPa. The unsteady-state, three dimensional Navier-Stokes equation was solved by using an edge-based finite element algorithm[42]. Time-varying boundary conditions at most of the boundaries were given by intravascular duplex Doppler measurements. The wall was modeled as rigid and the no-slip wall boundary condition was applied at the wall. The CFD software package used here is Feflo. It could be implemented for modeling of low speed incompressible and high-speed compressible fluid flow independently on computer platform or operating system. Two complete cardiac cycles were run and each cardiac cycle was discretized by 100 time steps in the CFD

analysis. The simulation was completed by using a 3GHz dual Xeon processor work station with 64GB of memory.

In our study, velocity and zero normal stress boundary conditions were used. At four of the five boundaries, a spatial velocity profile with uniform waveform was applied. The zero traction condition was prescribed for the branch left. The time dependent velocity profile was prescribed for the three of the four velocity boundaries using Doppler data measured inside the ascending aorta, right communicating carotid artery (RCCA) and the right subclavian artery (SCA). The velocity profile for the descending artery and left subclavian artery remain unclear due to low resolution or inaccessibility of Doppler measurements. By assuming identical WSS at each vessel, we can calculate the velocity for the descending artery according to the cube law:

$$\frac{4\mu Q_{asc}}{\pi {R_{asc}}^3} = \frac{4\mu Q_{des}}{\pi {R_{des}}^3} \quad \textbf{(4-1)}$$

Here $Q_{asc}$is measured as 6.113 cm^3/s. R_{asc} and R_{des} are 0.83 cm and 0.73 cm separately. According to equation 4-1, the time averaged flow rate of descending artery should be 4.159 cm^3/s.

While the spatial velocity profile over the cross section of each vessel is assumed to be uniform since the blood is leaving the heart, the temporal velocity waveforms of each vessel are pulsatile. Assuming that the arterial wall is rigid and conservation of mass is preserved, the temporal velocity waveforms should be identical in each branch. However, there is error associated with the measurement technique due to noise from the objects themselves and the

measuring equipment. Therefore, the obtained waveforms this condition will not be met identically. To ensure the assumption of conservation of mass and continuum mechanics, the velocity profile at each boundary is therefore rescaled using a representative waveform shape. This chosen waveform is measured at the location where is as close as possible to the aneurysm. To ensure that the time averaged flow rate at each boundary is preserved, the maximum and minimum velocity from the initial waveform are adjusted slightly to fit the new waveform. In this study, the waveform measured from right subclavian artery was chosen as the representative waveform shape due to its location and clarity compared with other obtained waveforms. The waveform is shown in Figure 5. This rescaling process was done using Matlab software (MATLAB and Statistics Toolbox Release 2012b, The MathWorks, Inc., Natick, Massachusetts, United States). In Appendix A.1, the time-dependent flow rate at each branch for one cardiac cycle are given.

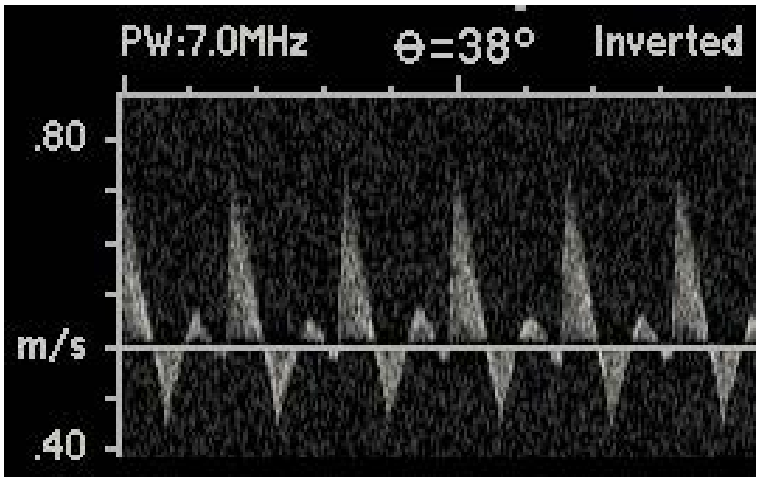

Figure 5. The time-dependent velocity waveform of subclavian carotid artery

The only boundary condition left to determinate is the one for left subclavian artery. Due to the difficulties of measuring time varied pressure profile for this model, a “traction free” boundary condition is chosen to be prescribed. It is still feasible if we use uniform WSS assumption to calculate the theoretical velocity boundary condition at left subclavian artery and leave the descending artery as traction free. In a result, the boundary conditions applied on Test Case 2 are shown in Figure 5.

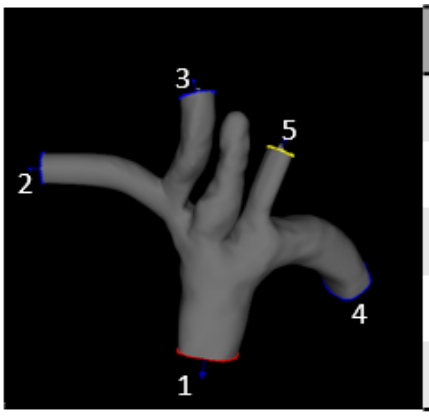

Artery	Boundary
1. Ascending Artery	TVU
2. Right Subclavian Artery	TVU
3. Right Communicating Carotid Artery	TVU
4. Descending Artery	TVU
5. Left Subclavian Artery	Traction Free

Figure 6. Boundary conditions applied on each inlet (1) and outlest (2-5) for Test Case 2. A time varying uniform (TVU) waveform was applied at four boundaries and a zero traction condition was applied at the remaining outlet.

4.3 RESULT

In this section, the Cebral flow types generated for Test Case 2 were identified based on CFD results for the streamlines. With the high pressure condition produced by the attached venous system, a fully prograde flow condition was generated. In Figure 7, the streamlines for the high AR and low AR geometries are given. In the high AR case, the jet flow into the sac first

impinged on the neck area. As the impingement point was close to the aneurysm inlet, a small amount of flow was not able to enter the sac but directly flowed into the downstream branches. The central jet then impinged on the wall of the aneurysm and split, forming a Type 2 flow. In the low AR case, the jet flow also impinged twice inside the aneurysm. However, as a result of the low AR geometry, the second impingement point was in the side of dome area of the aneurysm and thus produced a Type 1 flow. The streamline helps to give reasonable perspective of the flow type, but other methods of visualizing the flow are also needed to make a solid conclusion. Thus, figures of velocity iso-surface and vortex core line are also made for identifying the location of impingement point and the number of vortices that were generated during the whole cardiac cycle.

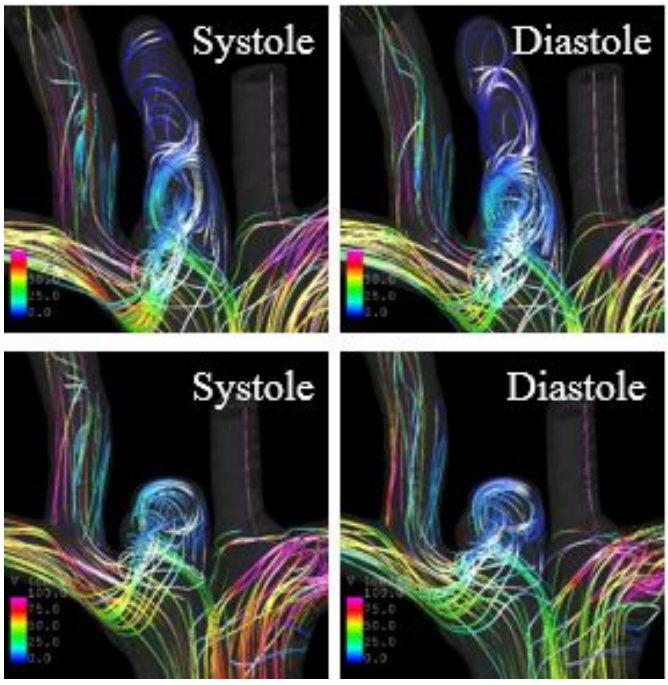

Figure 7. Upper row: Streamline of high AR case in the period of systole and diastole; Lower row: Streamline of low AR case in the period of systole and diastole.

Normally, the flow rate inside the sac is very low away from the high flow jet. Thus, a threshold of velocity is set to visualize the jet flow and obtain the impingement point. In our case, this threshold was set as 15 cm/s and the inflow jet penetration for both high AR and low AR case are shown in Figure 8. Although two impingement points were recognized in Figure 7, only one impingement point could be observed in Figure 7. Since the first impingement point only caused minor jet flow division and barely influenced the flow pattern formed inside the sac, it made the second impingement point more important for investigation. In Figure 8, the impingement point for the high AR case can be seen in the body area of the aneurysm while that for the low AR case was in the dome area of the aneurysm. The result is consisting with the observation in the figures of streamline.

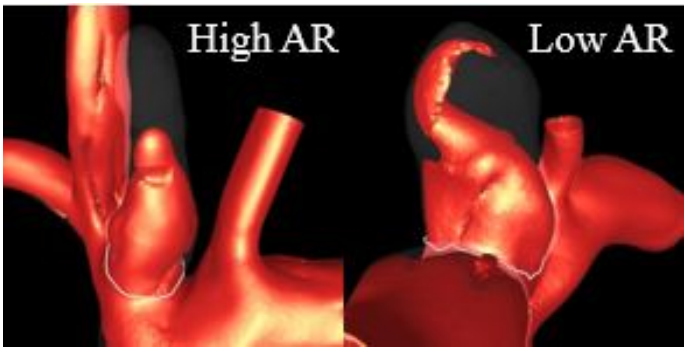

Figure 8. Left: The impingement point of high AR case was in the body area of the aneurysm; Right: The impingement point of low AR case was in the dome area of the aneurysm.

In Figure 9, the vortex core line in the high AR case was destroyed and created periodically. It started with a very short length at systole and then grew longer along with the deceleration of blood flow rate during the transition to diastole. At diastole, another vortex core line appeared which was fragmented and did not form a single core line. In the low AR case, one

clear vortex core line was formed and maintained during the whole cardiac cycle. Although the orientation of the core line kept changing, the length of the core line remained almost the same. This indicated that only one vortex was generated in the low AR case, which supported the conclusion that the flow pattern should be classified as Type 1 flow.

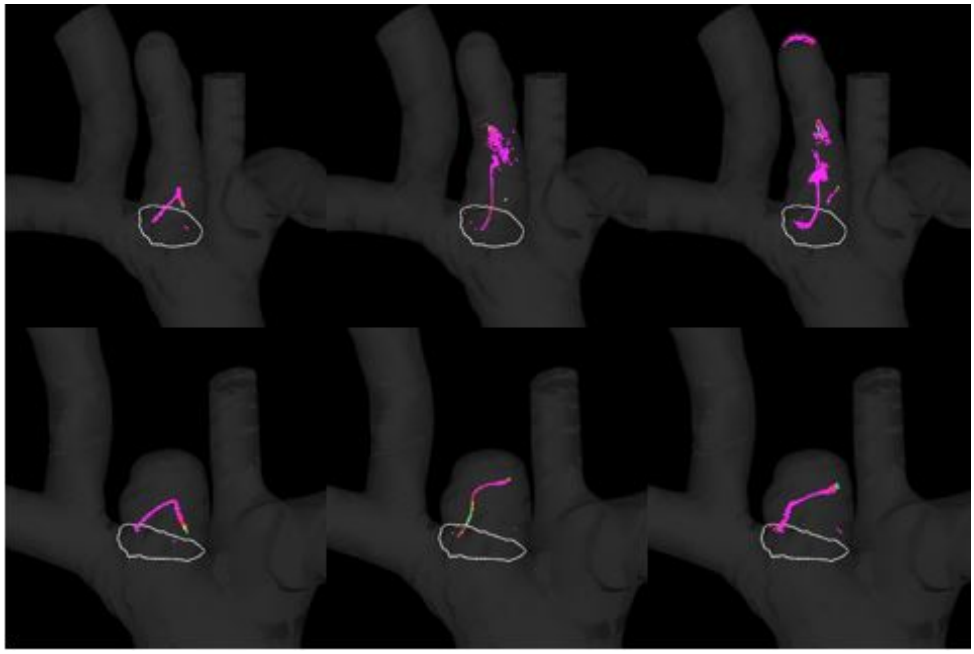

Figure 9. Upper row: The development of core line length in high AR case during one cardiac cycle; Lower row: The development of core line length in high AR case during one cardiac cycle.

The robustness of Test Case 2 was evaluated by modifying the original model and comparing the consistency of the results. In both high AR and low AR case, although slight differences were noticeable, a good agreement of the locations of impingement point and the developing trend of the streamline between the modified and original model has been reached, Figure 10 and 11. The locations of the impingement point were all in the body area of the

aneurysm in the high AR case while that for low AR case was in dome area, Figure 12 and 13. Comparing the vortex core lines between the original and modified geometries in Figure 14 and 15, it can be seen the development of vortex was also qualitatively similar. In particular, the formation and growth of one short core line could be noticed in all high AR cases while one stable core line remains intact in all low AR cases.

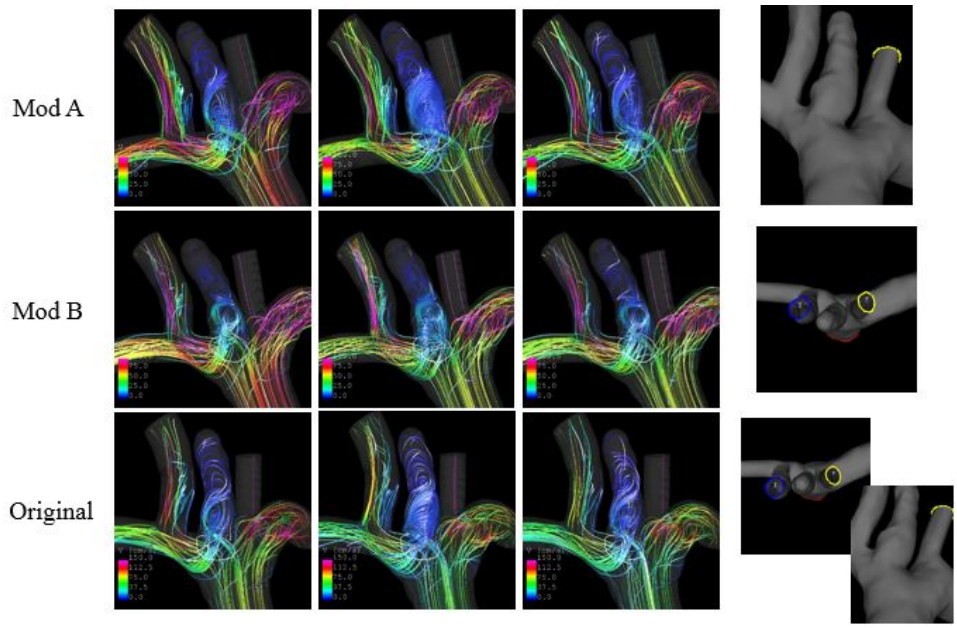

Figure 10. Robustness test for high AR cases. Mod A: The streamline of the bottlenecked aneurysm; Mod B: The streamline of the inclined aneurysm; Original: The streamline of the original aneurysm.

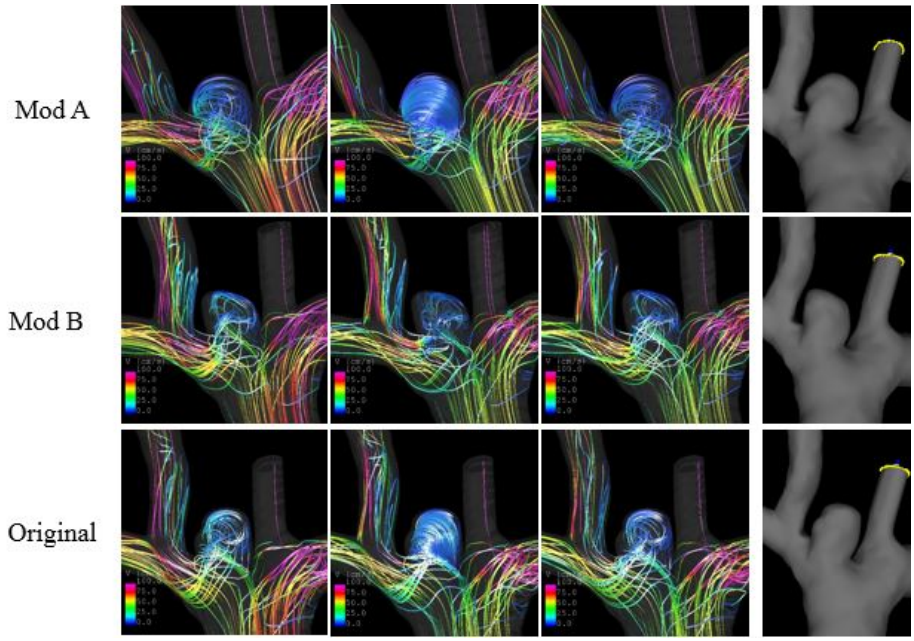

Figure 11**.** Robustness test for low AR cases. Mod A: The streamline of the bottlenecked aneurysm; Mod B: The streamline of the inclined aneurysm; Original: The streamline of the original aneurysm.

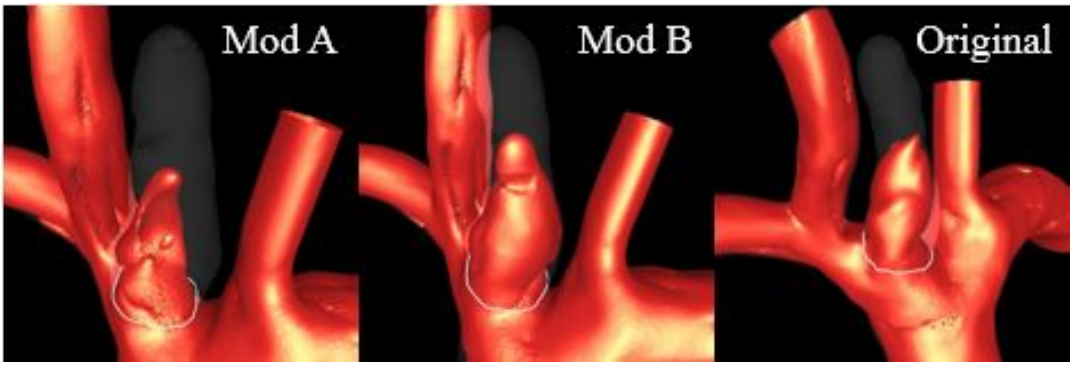

Figure 12. Robustness test for high AR cases. Mod A: The impingement point of the bottlenecked aneurysm; Mod B: The impingement point of the inclined aneurysm; Original: The impingement point of the original aneurysm.

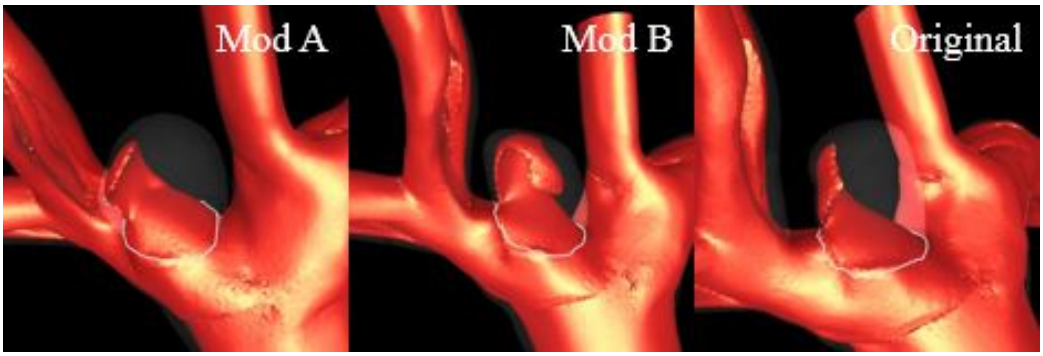

Figure 13. Robustness test for low AR cases. Mod A: The impingement point of the bottlenecked aneurysm; Mod B: The impingement point of the inclined aneurysm; Original: The impingement point of the original aneurysm.

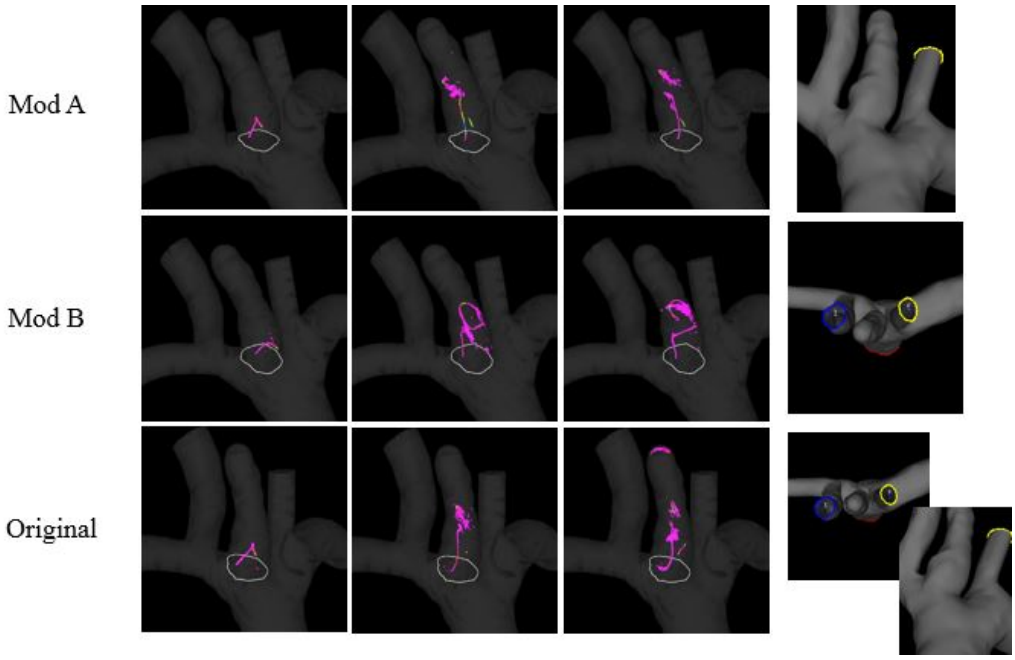

Figure 14. Robustness test for high AR cases. Mod A: The core line of the bottlenecked aneurysm; Mod B: The core line of the inclined aneurysm; Original: The core line of the original aneurysm.

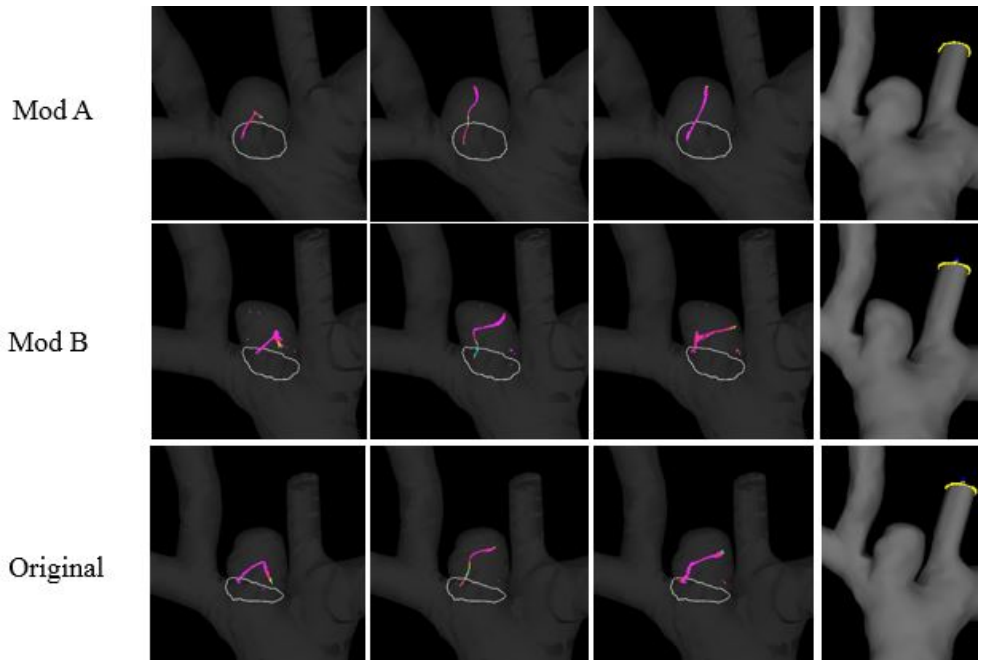

Figure 15. Robustness test for low AR case. Mod A: The core line of the bottlenecked aneurysm; Mod B: The core line of the inclined aneurysm; Original: The core line of the original aneurysm.

4.4 DISCUSSION AND LIMITATIONS

In our study, a new bifurcation rabbit aneurysm model was evaluated to assess the types of flow that could be generated and also to assess the robustness of flow type to perturbations in geometry. These results are consistent with results on an earlier bifurcation model (Test Case 1) and further support the value of these new high flow bifurcation-like rabbit models. In particular, we have shown here that Type 1 and Type 2 flows are successfully generated in the low AR and high AR case, respectively. Additionally, the flow type given by Test Case 2 is robust to perturbations in geometry and direction of the aneurysm. This result is consisting with the results from Test Case 1, which is also a high flow bifurcation-like rabbit aneurysm model with a slightly different location on the aortic arch and a lower aspect ratio sac geometry. Thus,

we can conclude that the flow types that could be generated in this novel bifurcation-like rabbit model are insensitive to the length of the sac found in this Case 2 model. Previously reported work on human cerebral aneurysms suggests aneurysms with more irregular shape are at greater risk of rupture[43][44]. Thus the irregular long rabbit aneurysm model considered here might be of special value for understanding this vulnerability.

Serval improvements could be made in the future study. The velocity boundary condition applied on the descending artery are prescribed using assumptions about WSS distribution across downstream vessels instead of an actual physical measurement. Although the calculated velocity boundary condition is not expected to cause significant error in the computational results, this should be confirmed in future studies if possible. Similarly, the measurement of pressure at the left subclavian artery is also desired.

Motivated by the desire to study the flow fields efficiently, and based on prior published results, our group chose to use rigid wall boundary conditions and neglected all the interactions between the arterial wall and the blood. With the development in hemodynamics, more accurate and feasible fluid-structure interaction model might be used to replace the rigid wall boundary condition. However, this is not expected to have a major impact on our results because the aneurysm wall rarely has elastin remaining and, likely as a result, demonstrates only a short toe region in the loading curve. Hence, the motion of the wall will be greatly diminished compared with healthy arteries.

The Cebral flow types were assessed for each study, largely based on the appearance of the streamlines. In the high AR case, although the vortex core lines were also given as a supplement, they were not very helpful for recognizing the number of vortices formed in one cardiac cycle due to the fragmentation of the core line. A quantitative study of the characteristic

flow is of interest for the further study. One improvement that could be made to provide more precise results is to use finer time steps. 100 time steps per cardiac cycle were used in this research. While this is consistent with prior work, such time steps may not be sufficient to catch higher frequency oscillations should they exist.

5.0 FUTURE STUDY: QUANTITAIVE STUDY OF CHARACTERISTIC FLOW

5.1 OVERVIEW

For investigating the relationship between characteristic hemodynamics and aneurysm geometry, a series of characteristic parameters such as AR, impingement region, oscillation index of jet flow is defined. Qualitative studies of these characteristic parameters have significantly facilitated the understanding of the initiation, growth and rupture of aneurysm. However, the ultimate goal for studying aneurysms is to predict the possibility of aneurysm rupture so that proper treatment could be advised for each specific patient. Although it has been clarified that the abnormal WSS could be one of the reason which lead to aneurysm rupture, the definition of "abnormal" is too general and subjective for evaluating the risk of rupture for each specific patient. Thus, quantitative criterions were introduced and associated with the rupture of aneurysm by preforming CFD analysis. Some quantitative study has already been done by Cebral, Byrn and Mut [8][45]. Strong evidence showed that rupture aneurysms shared similar values or fells in a certain range among some quantitative parameters. In this study, the most commonly used quantitative parameters such as POD, the number of POD, core line length, mean WSS, shear concentration index and inflow concentration index are described in the following sections. The values of these parameters from Test Case 2 are also given.

5.2 PARAMETERS USED IN QUANTITATIVE STUDY

5.2.1 Proper orthogonal decomposition

Proper orthogonal decomposition (POD) is one of the most efficient and robust methods to extract flow information. The basic idea of this method is to generate a series of orthogonal low dimensional basis, also recognized as modes, in order to describe a high dimensional dynamic system. Compared with other methods, POD is capable of representing the flow structure that contains most of the energy of the original system by using a linear combination of the modes. The number of POD normally regards to the number of modes that exist in the process. Large POD number indicates that frequent energy exchanging processes are occurring in the development of flow. Originally, the application of POD is basically in the reorganization or identification of the characteristics of one big data set, such as turbulent flow. However, Cebral's introduction of POD in the biomedical field is novel.

Mathematically, the velocity of a system can be represented as:

$$u(x, t_j) = \sum_{i}^{N} \alpha_i(t_j)\varphi_i(x), \qquad j = 1, \dots, N \tag{5-1}$$

where $\varphi_i(x)$ are the vector-based modes, $\alpha_i(t_j)$ are the scalar coefficients and N is the number of snapshots in the ensemble. The number of modes is recognized as NPOD in this paper.

The entropy S, which quantifies the average energy distributed among different modes is introduced here to measure the transient stability of the flow:

$$S = -\sum_{i=1}^{N} P_i \ln(P_i) \quad \textbf{(5-2)}$$

In this equation, P_i represents the corresponding energy contained in the ith mode. When the energy is transferred evenly over the modes, the entropy is maximized. In contrast, minimum entropy is obtained when the energy is concentrated in a single mode.

5.2.2 Core line length

Vortex core lines are the lines formed by sets of continuous points where the cross production of locally vorticity and velocity is zero:

$$\vec{\omega} \times \vec{v} = 0 \quad \textbf{(5-3)}$$

where $\vec{\omega}$ is the curl of the velocity. The numeric algorithm used to assess the core line contains a parallel search over different processors for tetrahedral elements which satisfied the equation above. Each processor formed and diagonalized the velocity gradient tensor in one element. By subtracting the velocity component in the direction of the vorticity, the reduced-velocities were

formed at every element node. All the points which contain zero reduced-velocity are marked and an approximating segment is drawn between each two adjacent points. The vortex core segments in each mesh element at the ith snapshot were added up together as the total length L_i. For quantifying the spatial complexity, the averaged vortex core line length over the N snapshots is:

$$\langle L \rangle = \frac{1}{N} \sum_{i=1}^{N} L_i \qquad \textbf{(5-4)}$$

By performing a statistical study of the core line length in all 210 IA geometries, Cebral concluded that complex flow (flow with more than one vortex) normally has longer core line length than simple flow (flow with just one vortex). Furthermore, rupture aneurysms are found to have longer core line length than unruptured aneurysms.

5.2.3 Mean wall shear stress

The mean wall shear stress (WSSMEAN) is defined as the mean value of the time averaged projection of the Cauchy stress vector on the aneurysm surface. Area of arterial wall with unusual high or low mean wall shear stress is suspected to have high possibility of rupture.

5.2.4 Inflow concentration index

Inflow concentration index (ICI) measured the concentration of the flow entering the aneurysm. It is represented as the ratio between the percentages of the flow rate that enters the aneurysm from the parent artery and the percentage of the aneurysm ostium area with positive inflow velocity.

$$ICI = \frac{Q_{in}/Q_v}{A_{in}/A_o} \quad \textbf{(5-5)}$$

Where Q_{in} is the inflow entering the artery, Q_v is the flow rate of the parent artery, A_{in} is the area of the inflow region and A_o is the area of the ostium surface.

5.2.5 Shear concentration index

Shear concentration index (SCI) is used to show the degree of concentration of the WSS distribution. Simply, SCI is noted as:

$$SCI = \frac{\frac{F_h}{A_h}}{\frac{F_a}{A_a}} \quad \textbf{(5-6)}$$

Where $\frac{F_h}{A_h}$ is the ratio of total viscous shear force and the area of high WSS region; $\frac{F_a}{A_a}$ is the ratio of total viscous shear force and the area of the whole sac.

5.3 QUANTITATIVE STUDY OF THE NEW RABBIT MODEL

In order to investigate the robustness of flow type in the novel rabbit model, two modifications of geometry were made (increase in bottleneck and increase in aneurysm inclination). In a qualitative analysis, the flow type was robust to these changes in geometry. However, further differences can be picked up in the quantitative study. There remains a pressing need to understand which of these flow parameters are important for the aneurysm wall biology and also what magnitudes of change are needed to impact the biology. None the less, for completeness we report the values of these parameters here as well as changes arising from the geometric perturbations. When further information is available, the importance of these changes in parameters can be assessed.

In our study, some quantitative parameters, including the entropy (Podent), number of modes (N POD), core line length (Lcore), inject concentration index (ICI) and the mean wall shear stress (MWSS), were calculated and compared for both modified and original models, Table 2. From Table 2, it can be seen that changes to core line length in Mod A relative to the original (control) are larger than in Mod B. One explanation is that the shape of the aneurysm determines the speed and cross sectional area of jet flow and thus effects the flow pattern produced in the sac. The close value in core line length from Mod B and original case (1.87 and 1.90 separately) also proved that the direction of aneurysm would not cause considerable changes in the inflow volume. However, the MWSS in Mod B decreased more than 50% compared with the original case while that in Mod A only decreased 15%. The directional change of aneurysm centerline created in Mod B generated more substantial variations in MWSS. Therefore, if the magnitude of MWSS is important in studies of the rabbit model, the orientation of aneurysm should be controlled. The exact range can be considered in a future

study and will depend on threshold values of MWSS. In this parameter investigated, the parameter most sensitive to geometric perturbations was the ICI which represents the concentration area of the jet flow. The value of ICI changed 24% and 40% representatively compared with the original case. The N POD and the Podent were not substantially affected by the geometric perturbations considered here. In conclusion, the impingement point and impingement area are more sensitive to the geometry of the sac than the other parameters such as those related to entropy. The MWSS and Lcore are more sensitive to the orientations of the sac considered here than the shape of the aneurysm. In the future, depending on the threshold values of these two parameters, it may be important to consider the sensitivity of the outcome to these parameters.

Table 2. Quantitative parameters of Test Case 2

Model	N POD	Podent	ICI	Lcore	MWSS
Mod A	2	0.37	0.019	1.87	12.76
Mod B	2	0.409	0.015	1.54	7.38
Original	2	0.39	0.025	1.9	15

Currently, the classification of flow type is still based on manly observation. It is possible that the subjective judgement may lead to considerable different conclusion of the flow type. Thus, quantitative parameters are expected to serve as objective criterions for the classification of flow type. For an instance, POD is one of the quantitative parameter that implemented to analysis turbulent flow. For a spherical velocity field, the first mode of POD is recognized as Dudley-James flow which has two simple axisymmetric swirling [46]. The second mode of POD

is a helical flow around the center axis [47]. When put the two major flow from different modes together, diverse results are observed due to different orientation of the swirling core line. For example, in our study, the N POD of low AR case and high AR case of Test Case 2 were both 2. However, the flow type that generated was Type 1 flow in low AR case and Type 2 flow in high AR case. Further study is needed to link quantitative parameters with the classification of flow type.

APPENDIX A

DATA USED IN THE RESEARCH

A.1 TABLE 3. TIME AVERAGED VELOCITY BOUNDARY CONDITION

Ascending Artery (cm/s)	Descending Artery (cm/s)	SCA (cm/s)	RCCA (cm/s)
31.17807	29.7682	6.274667	4.616327
31.32275	29.87917	6.294626	4.63188
31.21614	29.7974	6.279919	4.62042
31.10954	29.71563	6.265212	4.60896
31.00294	29.63385	6.250505	4.5975
32.14513	30.51	6.408081	4.720285
36.4093	33.78092	6.996364	5.178682
40.67347	37.05185	7.584646	5.63708
42.06694	38.12074	7.776889	5.786877
43.23959	39.02024	7.938667	5.912937
43.92491	39.54593	8.033212	5.986608
44.24472	39.79125	8.077333	6.020987
44.43758	39.93919	8.103941	6.04172
44.16497	39.73008	8.066331	6.012414
43.89236	39.52096	8.028722	5.983109
43.09091	38.90619	7.918155	5.896953
42.20132	38.22382	7.795428	5.801323
41.29647	37.52973	7.670594	5.704051
40.37634	36.82393	7.543655	5.605138
39.51013	36.15948	7.424152	5.51202
38.96734	35.74312	7.34927	5.453671
38.42456	35.32677	7.274387	5.395322
37.81613	34.86006	7.19045	5.329917
37.18981	34.37963	7.104042	5.262587
36.59553	33.92378	7.022056	5.198702
36.04399	33.5007	6.945965	5.139411

TABLE 3. (CONT'D)

34.88945	32.61509	6.786686	5.015299
34.28989	32.15519	6.703972	4.950847
33.69687	31.70029	6.622159	4.887097
33.10646	31.24741	6.540706	4.823629
32.58571	30.84795	6.468863	4.767648
32.19033	30.54467	6.414317	4.725144
31.79495	30.24138	6.35977	4.682641
31.45329	29.97931	6.312635	4.645913
31.11163	29.71723	6.265501	4.609185
30.75504	29.4437	6.216305	4.570851
30.39015	29.1638	6.165966	4.531626
30.03622	28.89231	6.117137	4.493578
29.70966	28.64182	6.072086	4.458474
29.38311	28.39133	6.027034	4.423369
29.12469	28.19311	5.991384	4.395589
28.87152	27.9989	5.956456	4.368373
27.84087	27.20833	5.814269	4.257579
26.22712	25.97046	5.591637	4.084102
24.962	25.00002	5.417101	3.948102
24.97517	25.01012	5.418918	3.949517
24.98833	25.02022	5.420734	3.950932
25.182	25.16878	5.447453	3.971752
25.40575	25.34042	5.478321	3.995805
25.88379	25.7071	5.54427	4.047193
26.6161	26.26883	5.645299	4.125916
27.32613	26.81348	5.743256	4.202245
27.90253	27.25562	5.822775	4.264207
28.47892	27.69775	5.902294	4.326169
28.8717	27.99905	5.956481	4.368393
29.21441	28.26192	6.00376	4.405234
29.50322	28.48347	6.043605	4.436282
29.72019	28.6499	6.073538	4.459606
29.95691	28.83148	6.106197	4.485053
30.45043	29.21004	6.174282	4.538106
30.94394	29.5886	6.242367	4.591159
31.09413	29.70381	6.263086	4.607304
31.10699	29.71367	6.26486	4.608686
31.44417	29.97231	6.311377	4.644932
32.36513	30.67876	6.438433	4.743936
33.2861	31.3852	6.565488	4.842939

TABLE 3. (CONT'D)

33.47874	31.53297	6.592065	4.863648
33.67138	31.68074	6.618642	4.884357
33.91715	31.86927	6.652548	4.910777
34.19244	32.08043	6.690527	4.940371
34.39582	32.23644	6.718586	4.962235
34.41944	32.25455	6.721843	4.964773
34.44305	32.27267	6.725101	4.967311
34.34574	32.19803	6.711677	4.956851
34.23914	32.11625	6.69697	4.945391
34.19345	32.08121	6.690667	4.94048
34.19345	32.08121	6.690667	4.94048
34.10208	32.01112	6.678061	4.930657
33.67566	31.68402	6.619232	4.884817
33.24924	31.35693	6.560404	4.838977
32.9142	31.09993	6.514182	4.80296
32.59439	30.85461	6.470061	4.768581
32.16797	30.52752	6.411232	4.722741
31.63495	30.11865	6.337697	4.665441
31.17807	29.7682	6.274667	4.616327
31.17807	29.7682	6.274667	4.616327
31.17807	29.7682	6.274667	4.616327
31.17807	29.7682	6.274667	4.616327
31.17807	29.7682	6.274667	4.616327
31.0867	29.6981	6.262061	4.606504
30.87349	29.53456	6.232646	4.583585
30.67551	29.38269	6.205333	4.562302
30.67551	29.38269	6.205333	4.562302
30.67551	29.38269	6.205333	4.562302
30.67551	29.38269	6.205333	4.562302
30.67551	29.38269	6.205333	4.562302
30.75165	29.4411	6.215838	4.570487
30.96486	29.60465	6.245253	4.593407
31.17807	29.7682	6.274667	4.616327

BIBLIOGRAPHY

[1] R. D. Brown and J. P. Broderick, “Unruptured intracranial aneurysms: Epidemiology, natural history, management options, and familial screening,” Lancet Neurol., vol. 13, no. 4, pp. 393–404, 2014.

[2] Y.-G. Jeong, Y.-T. Jung, M.-S. Kim, C.-K. Eun, and S.-H. Jang, “Size and location of ruptured intracranial aneurysms.,” J. Korean Neurosurg. Soc., vol. 45, no. 1, pp. 11–5, 2009.

[3] I. Amber, S. Mohan, and P. Nucifora, “Intracranial Aneurysms. A Game of Millimeters,” Acad. Radiol., vol. 22, no. 8, pp. 1020–1023, 2015.

[4] H. Baek, M. V. Jayaraman, and G. E. Karniadakis, “Wall shear stress and pressure distribution on aneurysms and infundibulae in the posterior communicating artery bifurcation,” Ann. Biomed. Eng., vol. 37, no. 12, pp. 2469–2487, 2009.

[5] J. R. Cebral et al., “Analysis of hemodynamics and wall mechanics at sites of cerebral aneurysm rupture,” J. Neurointerv. Surg., vol. 7, no. 7, pp. 530–536, 2015.

[6] H. Meng, V. M. Tutino, J. Xiang, and A. Siddiqui, “High WSS or Low WSS? Complex interactions of hemodynamics with intracranial aneurysm initiation, growth, and rupture: Toward a unifying hypothesis,” Am. J. Neuroradiol., vol. 35, no. 7, pp. 1254–1262, 2014.

[7] J. R. Cebral, F. Mut, J. Weir, and C. M. Putman, “Association of hemodynamic characteristics and cerebral aneurysm rupture,” Am. J. Neuroradiol., vol. 32, no. 2, pp. 264–270, 2011.

[8] G. Byrne, F. Mut, and J. Cebral, “Quantifying the large-scale hemodynamics of intracranial aneurysms,” Am. J. Neuroradiol., vol. 35, no. 2, pp. 333–338, 2014.

[9] O. Naggara et al., “A new canine carotid artery bifurcation aneurysm model for the evaluation of neurovascular devices,” Am. J. Neuroradiol., vol. 31, no. 5, pp. 967–971, 2010.

[10] A. Simgen et al., “Evaluation of a newly designed flow diverter for the treatment of intracranial aneurysms in an elastase-induced aneurysm model, in New Zealand white rabbits,” Neuroradiology, vol. 56, no. 2, pp. 129–137, 2014.

[11] F. Bouzeghrane, O. Naggara, D. F. Kallmes, A. Berenstein, and J. Raymond, “In vivo experimental intracranial aneurysm models: A systematic review,” Am. J. Neuroradiol., vol. 31, no. 3, pp. 418–423, 2010.

[12] S. Appanaboyina, F. Mut, R. Löhner, C. Putman, and J. Cebral, “Simulation of intracranial aneurysm stenting: Techniques and challenges,” Comput. Methods Appl. Mech. Eng., vol. 198, no. 45–46, pp. 3567–3582, 2009.

[13] J. J. Schneiders et al., “Rupture-associated changes of cerebral aneurysm geometry: High-resolution 3D imaging before and after rupture,” Am. J. Neuroradiol., vol. 35, no. 7, pp. 1358–1362, 2014.

[14] and T. W. Takehiro Naito, Shigeru Miyachi, Noriaki Matsubara, Haruo Isoda, Takashi Izumi, Kenichi Haraguchi, Ichiro Takahashi, Katsuya Ishii, “Magnetic resonance uid dynamics for intracranial aneurysmscomparison with computed aid dynamics,” Acta Neurochir. (Wien)., 2012.

[15] Z. Zeng et al., “Sensitivity of CFD based hemodynamic results in rabbit aneurysm models to idealizations in surrounding vasculature.,” J. Biomech. Eng., vol. 132, no. 9, p. 91009, 2010.

[16] A. M. G. and A. S. S. Ramalho, A. Moura, “Sensitivity to outflow boundary conditions and level of geometry description for a cerebral aneurysm,” Int. j. numer. method. biomed. eng., vol. 26, no. 1, pp. 807–827, 2012.

[17] J. R. Cebral, M. A. Castro, J. E. Burgess, R. S. Pergolizzi, M. J. Sheridan, and C. M. Putman, “Characterization of cerebral aneurysms for assessing risk of rupture by using patient-specific computational hemodynamics models,” Am. J. Neuroradiol., vol. 26, no. 10, pp. 2550–2559, 2005.

[18] L. Yan, Y. Q. Zhu, M. H. Li, H. Q. Tan, and Y. S. Cheng, “Geometric, hemodynamic, and pathological study of a distal internal carotid artery aneurysm model in dogs,” Stroke, vol. 44, no. 10, pp. 2926–2929, 2013.

[19] Y. H. Ding, R. Kadirvel, D. Dai, and D. F. Kallmes, “Creation of bifurcation-type elastase-induced aneurysms in rabbits,” Am. J. Neuroradiol., vol. 34, no. 2, pp. 1–3, 2013.

[20] Y. H. Ding et al., “Long-term patency of elastase-induced aneurysm model in rabbits,” Am. J. Neuroradiol., vol. 27, no. 1, pp. 139–141, 2006.

[21] Z. Zeng et al., “Hemodynamics and anatomy of elastase-induced rabbit aneurysm models: Similarity to human cerebral aneurysms?,” Am. J. Neuroradiol., vol. 32, no. 3, pp. 595–601, 2011.

[22] I. A. de Oliveira, “Main Models of Experimental Saccular Aneurysm in Animals,” InTech, vol. Chapter 3, 2012.

[23] J. B. Casals et al., “The use of animal models for stroke research: A review,” Comp. Med., vol. 61, no. 4, pp. 305–313, 2011.

[24] T. P. Lee and B. L. Chiang, “Sex differences in spontaneous versus induced animal models of autoimmunity,” Autoimmun. Rev., vol. 11, no. 6–7, pp. A422–A429, 2012.

[25] S. Anidjar, J. L. Salzmann, D. Gentric, P. Lagneau, J. P. Camilleri, and J. B. Michel, “Elastase-induced experimental aneurysms in rats.,” Circulation, vol. 82, no. 3, pp. 973–981, 1990.

[26] C. N. Ionita et al., “The asymmetric vascular stent: Efficacy in a rabbit aneurysm model,” Stroke, vol. 40, no. 3, pp. 959–965, 2009.

[27] and S. G. Zarins, Christopher K., Chengpei Xu, “Aneurysmal enlargement of the aorta during regression of experimental atherosclerosis,” J. Vasc. Surg., vol. 15.1, 1992.

[28] T. F. Massoud, G. Guglielmi, C. Ji, F. Viñuela, and G. R. Duckwiler, “Experimental saccular aneurysms - I. Review of surgically-constructed models and their laboratory applications,” Neuroradiology, vol. 36, no. 7, pp. 537–546, 1994.

[29] D. F. Kallmes et al., “Histologic evaluation of platinum coil embolization in an aneurysm model in rabbits,” Radiology, vol. 213, no. 1, pp. 217–222, 1999.

[30] C. M. Cawley, R. C. Dawson, G. Shengelaia, G. Bonner, D. L. Barrow, and A. R. T. Colohan, “Arterial saccular aneurysm model in the rabbit,” Am. J. Neuroradiol., vol. 17, no. 9, pp. 1761–1766, 1996.

[31] H. J. Cloft et al., “Endovascular creation of an in vivo bifurcation aneurysm model in rabbits.,” Radiology, vol. 213, no. 1, pp. 223–228, 1999.

[32] D. D. and A. M. R. Zijing Zeng, David F. Kallmes, Yong Hong Ding, Ramanathan Kadirvel, Debra A. Lewis, “Hemodynamics of Elastase-Induced Aneurysms in Rabbit: A New High Flow Bifurcation Model,” ASME 2011 Summer Bioeng. Conf., 2011.

[33] M. J. Durka, “A COMPUTATIONAL PARAMETRIC STUDY OF THE RELATIONSHIP BETWEEN,” 2013.

[34] T. F. I. Inc., “Blood- The Human Heart,” 2009. .

[35] N. Shahcheraghi, H. a Dwyer, a Y. Cheer, a I. Barakat, and T. Rutaganira, “Unsteady and three-dimensional simulation of blood flow in the human aortic arch.,” J. Biomech. Eng., vol. 124, no. 4, pp. 378–387, 2002.

[36] B. Liu, J. Zheng, R. Bach, and D. Tang, “Influence of model boundary conditions on blood flow patterns in a patient specific stenotic right coronary artery.,” Biomed. Eng. Online, vol. 14 Suppl 1, no. Suppl 1, p. S6, 2015.

[37] P. R. Painter, P. Edén, and H.-U. Bengtsson, “Pulsatile blood flow, shear force, energy dissipation and Murray’s Law.,” Theor. Biol. Med. Model., vol. 3, p. 31, 2006.

[38] G. S. Kassab and Y. C. B. Fung, “The pattern of coronary arteriolar bifurcations and the uniform shear hypothesis,” Ann. Biomed. Eng., vol. 23, no. 1, pp. 13–20, 1995.

[39] P. K. Siogkas et al., “Blood flow in arterial segments: rigid vs. deformable walls simulations,” J. Serbian Soc. Comput. Mech., vol. 5, no. 1, pp. 69–77, 2011.

[40] M. J. Durka, Q. Yang, G. Rettig, D. F. Kallmes, and J. R. Cebral, “A NEW RABBIT MODEL FOR INVESTIGATION OF HUMAN INTRACRANIAL ANEURYSMS,” no. April, 2017.

[41] W. Brinjikji, H. J. Cloft, and D. F. Kallmes, “Difficult aneurysms for endovascular treatment: Overwide or undertall?,” Am. J. Neuroradiol., vol. 30, no. 8, pp. 1513–1517, 2009.

[42] H. Luo, J. Baum, and R. Lohner, “Edged-Based Finite Element Scheme for the Euler Equations,” AIAA J., vol. 32, no. No.6, pp. 1183–1189, 1994.

[43] A. E. Lindgren et al., “Irregular Shape of Intracranial Aneurysm Indicates Rupture Risk Irrespective of Size in a Population-Based Cohort,” Stroke, vol. 47, no. 5, pp. 1219–1226, 2016.

[44] M. D. Motohiro Nomura, M.D., Sinya Kida, M.D., Naoyuki Uchiyama, M.D., Tetsumori Yamashima, M.D., Jun Yoshikawa, M.D., Junkoh Yamashita, M.D., and Osamu Matsui, “Irregular-shaped ruptured aneurysms: pseudoaneurysm formation in a thrombus at rupture site,” J. Neurosurg., vol. 93, no. 6, pp. 998–1002, 2000.

[45] J. R. Cebral, F. Mut, J. Weir, and C. Putman, “Quantitative characterization of the hemodynamic environment in ruptured and unruptured brain aneurysms,” Am. J. Neuroradiol., vol. 32, no. 1, pp. 145–151, 2011.

[46] M. L. D. and R. W. James, “Time-Dependent Kinematic Dynamos with Stationary Flows,” Proc. R. Soc. London. Ser. A, Math. Phys., vol. No.425, pp. 407–429, 1989.

[47] D. Hatch, “Application of Proper Orthogonal Decomposition to Analysis of Turbulence Dynamics,” 2014.